Journal of Materials Chemistry A

ROYAL SOCIETY OF CHEMISTRY

PAPER

View Article Online
View Journal | View Issue



Cite this: J. Mater. Chem. A, 2025, 13, 24772

# Synergistic bulk–interface stabilization of single-crystal cobalt-free high-nickel cathodes *via* a fast-ionic-conductor coating

Hailan Feng,[ad] Yuxing Xu,[ad] Ying Hou,[ac] Fuchang Zhuge*[e] and Qiangqiang Tan *[abd]

Single-crystal, cobalt-free, high-nickel $LiNi_{0.9}Mn_{0.1}O_2$ cathodes represent one of the most promising candidates for next-generation batteries, offering both high energy density and low cost. However, the cathodes suffer from rapid capacity decay in the highly delithiated state due to detrimental phase transitions, interfacial degradation, and oxygen loss. This work demonstrates a multifunctional $Li_{1.3}W_{0.15}Ti_{1.7}(PO_4)_3$ (LWTP) coating strategy that simultaneously addresses bulk and interfacial instability. The optimized 0.3 wt% LWTP-coated cathode delivers exceptional electrochemical performance, including an initial capacity of 214.1 mA h $g^{-1}$ at 4.5 V (compared to 208.2 mA h $g^{-1}$ for the bare cathode) and 15.9% improved capacity retention after 100 cycles, along with outstanding rate capability of 167.8 mA h $g^{-1}$ at 4.3 V and at a high rate of 3C (compared to 140.2 mA h $g^{-1}$ for the bare cathode). Comprehensive structural characterization reveals the coating's stabilization effects, including reduced $Li^+/Ni^{2+}$ cation mixing and suppression of rock-salt phase formation. Interfacial analyses demonstrate substantially lower charge transfer resistance and the formation of a stable cathode–electrolyte interphase. Mechanistic investigations demonstrate that the LWTP coating functions as an efficient ion-conductive network, strengthens metal–oxygen bonds through W/Ti doping, mitigates oxygen release, and prevents microcrack propagation *via* strain regulation. This multifunctional coating strategy provides a scalable materials engineering solution for developing ultra-stable, high-energy-density cathodes for next-generation lithium-ion batteries.

Received 8th April 2025
Accepted 22nd June 2025

DOI: 10.1039/d5ta02791h

rsc.li/materials-a



## 1 Introduction

The global push toward low-carbon, green, and sustainable development has driven rapid growth in the new energy vehicle industry in recent years.[1,2] As the core component of electric vehicles (EVs), power batteries critically determine their energy density, driving range, safety, and cost-effectiveness.[3,4] Among the key factors influencing lithium-ion battery performance, cathode materials play a pivotal role.[5] Among the commercialized cathode materials, the layered $LiNi_xCo_yMn_zO_2$ (NCM, $x + y + z = 1$) is considered to be the most promising positive electrode material in terms of high energy density.[6,7] However, despite the advantages of high-nickel polycrystalline NCM, its widespread adoption is hindered by inherent drawbacks, including structural instability during cycling, rapid capacity degradation, and the high cost of cobalt.[8–10] In order to meet the growing demand for high-energy-density, low-cost, and safe battery systems, the development of high-performance, single-crystal, cobalt-free nickel-rich cathodes has become imperative.[11] Single-crystal $LiNi_xMn_{1-x}O_2$ (SC-NM, $0.9 \leq x \leq 1$) represents a promising candidate for Co-free cathodes.[12–15] The increased Ni content and absence of Co reduce costs while effectively improving the capacity of SC-NM cathode materials.[16] Moreover, their densely packed structure and superior mechanical stability enhance energy density and structural integrity.[17,18]

Nevertheless, despite mitigating grain-boundary-induced cracking (a common issue in polycrystalline cathodes), SC-NM still suffers from intragranular fractures under high-voltage operation, impeding $Li^+$ diffusion and triggering detrimental phase transitions.[19,20] Additionally, the highly reactive $Ni^{4+}$ species accelerates electrolyte decomposition, increasing interfacial resistance and exacerbating capacity fade.[13,21] Furthermore, the intrinsically slow $Li^+$ diffusion kinetics in micron-sized single-crystal particles results in poor rate capability.[22]

[a]State Key Laboratory of Mesoscience and Engineering, Institute of Process Engineering, Chinese Academy of Sciences, Beijing 100190, China. E-mail: qtan@ipe.ac.cn

[b]Center of Materials Science and Optoelectronics Engineering, University of Chinese Academy of Sciences, Beijing, 100049, China

[c]School of Chemical Engineering, University of Chinese Academy of Sciences, Beijing, 100049, China

[d]Hebei Engineering Research Center of Power and Energy Storage Battery Materials, Hebei Technology Innovation Center of Advanced Energy Materials, Hebei Manufacturing Industry Innovation Center of New Energy Materials and Key Equipment, Langfang Technological Service Center of Green Industry, Langfang 065001, China

[e]Gansu Daxiang Energy Technology Co. Ltd, Gansu 730913, China

These challenges significantly limit the practical application of SC-NM cathodes.

To address these issues, extensive research has focused on surface modification strategies.[23] Conventional coatings, such as metallic oxides ($Al_2O_3$, $TiO_2$, $MnO_2$, $ZrO_2$, $WO_3$, $B_2O_3$, $V_2O_5$, *etc.*),[23–30] metallic fluorides ($AlF_3$) and phosphates ($AlPO_4$, $Li_3PO_4$, $BPO_4$, *etc.*),[31–34] effectively suppresses electrolyte-induced corrosion of the electrode material, ensuring interfacial stability while simultaneously enhancing interfacial ion/charge transfer to improve both electronic and ionic conductivity.[35,36] Furthermore, they stabilize the bulk structure by mitigating phase-transition-induced stress during cycling, thereby promoting long-term electrochemical performance.[37] Du *et al.* successfully constructed an $AlPO_4$–$Li_3PO_4$ protective layer on the surface of single-crystal $LiNi_{0.8}Co_{0.1}Mn_{0.1}O_2$. The analysis revealed that $Li_3PO_4$ enhances interfacial $Li^+$ transport kinetics, whereas $AlPO_4$ mitigates lattice strain during cycling. The synergistic effect between $Li_3PO_4$ and $AlPO_4$ significantly improves the material's electrochemical performance.[32] Research on coating modifications for single-crystal $LiNi_{0.9}Mn_{0.1}O_2$ cathode materials remains relatively scarce in the literature. Recently, Ma *et al.* reported a study on Mg/Nb/Al co-doped and $Al_2O_3$/$LiAlO_2$ coated Ni-rich single-crystal $LiNi_{0.9}Mn_{0.1}O_2$. The modified cathode exhibits higher capacity and better capacity retention of 85.5% after 300 cycles, while the uncoated cathode quickly dropped to 10.6% at 1C.[38] Liu *et al.* proposed a LiF coating on $LiNi_{0.9}Mn_{0.1}O_2$; the LiF-modified material maintains a superior capacity retention of 85.8% after 100 cycles at 0.5C. However, its rate capacity remains unsatisfactory, retaining only 104.5 mA h·g$^{-1}$ at 5C.[39] While this coating system can improve surface stability to some extent, its low intrinsic activity and high electrical resistance significantly compromise the conductivity of Ni-rich layered cathodes, ultimately limiting their high specific capacity and rate performance. Fast-ion conductors ($Li_4Ti_5O_{12}$, $Li_3V_2(PO_4)_3$, $Li_{1.3}Al_{0.3}Ti_{1.7}(PO_4)_3$, *etc.*) have gained attention for their balanced ionic transport and chemical inertness,[40–42] Notably, NASICON-type $LiTiM(PO_4)_3$ (M = $Y^{3+}$, $Zr^{4+}$, $Al^{3+}$, $Ta^{5+}$ and $Nb^{5+}$, *etc.*) coatings exhibit exceptional ionic conductivity and stability, significantly enhancing high-voltage cycling performance.[43–45] For instance, Fan *et al.* demonstrated that a $Li_{1.4}Y_{0.4}Ti_{1.6}PO_4$ coating effectively suppresses intragranular cracking and parasitic reactions in the single-crystal $LiNi_{0.88}Co_{0.09}Mn_{0.03}O_2$ cathode material, alleviating intragranular/intergranular cracking and preventing parasitic cathode/electrolyte reactions during delithiation/lithiation processes.[46]

Herein, we designed a modification strategy to develop a homogeneous fast-ion-conducting network on single-crystal $LiNi_{0.9}Mn_{0.1}O_2$ (SNM9) particles through a $Li_{1.3}W_{0.15}Ti_{1.7}(PO_4)_3$ (LWTP) coating. The designed LWTP framework not only facilitates lithium-ion transport but also enables beneficial W/Ti doping in the subsurface region, synergistically strengthening metal–oxygen bonding while reducing $Li^+$/$Ni^{2+}$ cation mixing. This synergistic modification effectively suppresses detrimental phase transformations and minimizes lattice oxygen loss, thereby preserving superior structural stability. The LWTP-modified SNM9 demonstrates enhanced electronic conductivity and improved $Li^+$ diffusion coefficients, contributing to exceptional electrochemical performance. Furthermore, the LWTP layer establishes an electrochemically stable interface that effectively mitigates cathode–electrolyte side reactions and prevents microcrack initiation, maintaining both structural and interfacial integrity even under high-voltage operation.

# 2 Experimental section

## 2.1 Preparation of materials

**2.1.1 Synthesis of $LiNi_{0.9}Mn_{0.1}O_2$.** The spherical precursor $Ni_{0.9}Mn_{0.1}(OH)_2$ (denoted as PNM9) was synthesized *via* a coprecipitation method. An aqueous mixed metal salt solution (2.0 mol L$^{-1}$) was prepared by dissolving $NiSO_4 \cdot 6H_2O$ and $MnSO_4 \cdot H_2O$ in a 9 : 1 molar ratio in deionized water. Simultaneously, stoichiometric NaOH solution (precipitating agent) and $NH_3 \cdot H_2O$ solution (chelating agent, 4.0 mol L$^{-1}$) were continuously pumped into the reaction system under a nitrogen atmosphere. The reaction was conducted in a water bath maintained at 55 °C, with the precursor solution pH stabilized at 11.6. The resulting precipitate was filtered, repeatedly washed with deionized water to remove impurities, and vacuum-dried at 120 °C for 10 h. The dried precursor was then thoroughly mixed with a 5% excess of LiOH *via* ball milling for 4 h. The mixture was subsequently calcined at 870 °C under oxygen flow for 10 h to obtain the final cathode material, labeled as SNM9.

**2.1.2 Synthesis of $Li_{1.3}W_{0.15}Ti_{1.7}(PO_4)_3$ coated $LiNi_{0.9}Mn_{0.1}O_2$.** The SNM9 powder was dispersed in deionized water at a mass ratio of 9 : 1. Stoichiometric amounts of $WO_3$, $TiO_2$, $LiNO_3$, and $NH_4H_2PO_4$ were then added to the suspension, followed by vigorous stirring for 30 minutes at room temperature. The mixture was subsequently heated to 80 °C to evaporate the solvent completely. After drying, the resulting powder was calcined at 820 °C for 10 h under flowing oxygen to obtain $Li_{1.3}W_{0.15}Ti_{1.7}(PO_4)_3$-coated single-crystal $LiNi_{0.9}Mn_{0.1}O_2$ particles. The final products were labeled based on the weight percentage of $Li_{1.3}W_{0.15}Ti_{1.7}(PO_4)_3$ (LWTP) relative to SNM9: SNM9@LWTP0.15 (0.15 wt% LWTP), SNM9@LWTP0.3 (0.3 wt% LWTP), and SNM9@LWTP0.45 (0.45 wt% LWTP).

## 2.2 Characterization of materials

X-ray diffraction (XRD) analysis was performed using a Shimadzu 7000S/L diffractometer. The morphological and microstructural characteristics of the samples were examined by scanning electron microscopy (SEM, Hitachi S-4800) and transmission electron microscopy (TEM, FEI Tecnai F20). Surface elemental composition was determined by energy-dispersive X-ray spectroscopy (EDS). The chemical states of surface elements were analyzed using X-ray photoelectron spectroscopy (XPS, AXIS SUPRA+). Particle size distribution was measured by laser diffraction (Mastersizer 2000, Dandong Bettersize Instruments). Differential electrochemical mass spectrometry (DEMS) measurements were conducted using a QMG220 system (Pfeiffer Vacuum) with argon carrier gas at a flow rate of 0.8 ml min$^{-1}$.

### 2.3 Electrochemical tests

The electrochemical properties of the samples were measured using CR2025 half-cells. The electrode slurry was prepared by mixing 92 wt% active material, 5 wt% acetylene black, and 3 wt% poly(vinylidene fluoride) (PVDF) in *N*-methyl-2-pyrrolidinone (NMP). The CR2025 coin cells were assembled with the prepared electrode (cathode), Li metal as the reference and counter electrode, a separator (Celgard 2400 porous polypropylene film), and electrolytes (appropriate electrolyte of 1 M $LiPF_6$ in a mixture of EC/DMC/EMC). The charge and discharge performance was monitored on a Xinwei CT2001C battery testing system (Shenzhen, China). The EIS (0.01 Hz–100 kHz) and CV (scan rate of 0.1 mV $s^{-1}$) curves of the material were measured on an electrochemical workstation (CHI660E, Shanghai, China).

## 3 Results and discussion

### 3.1 Morphology and structural analysis

The modification strategy to coat SNM9 cathode particles with LWTP *via* a combined wet coating and thermal heating

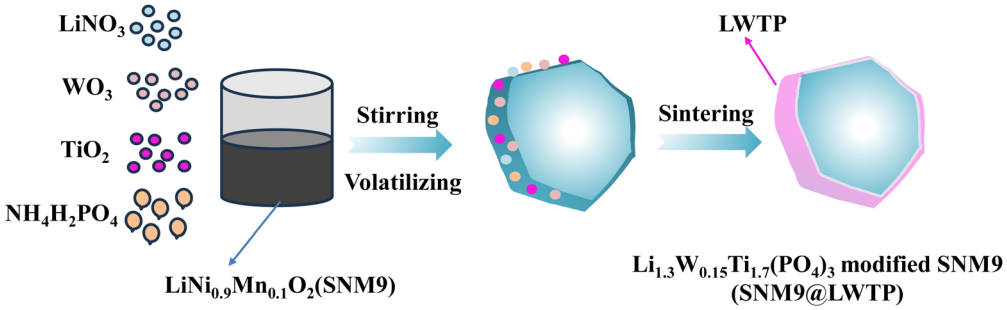


Fig. 1 Synthesis diagram of SNM9 coated with LWTP.

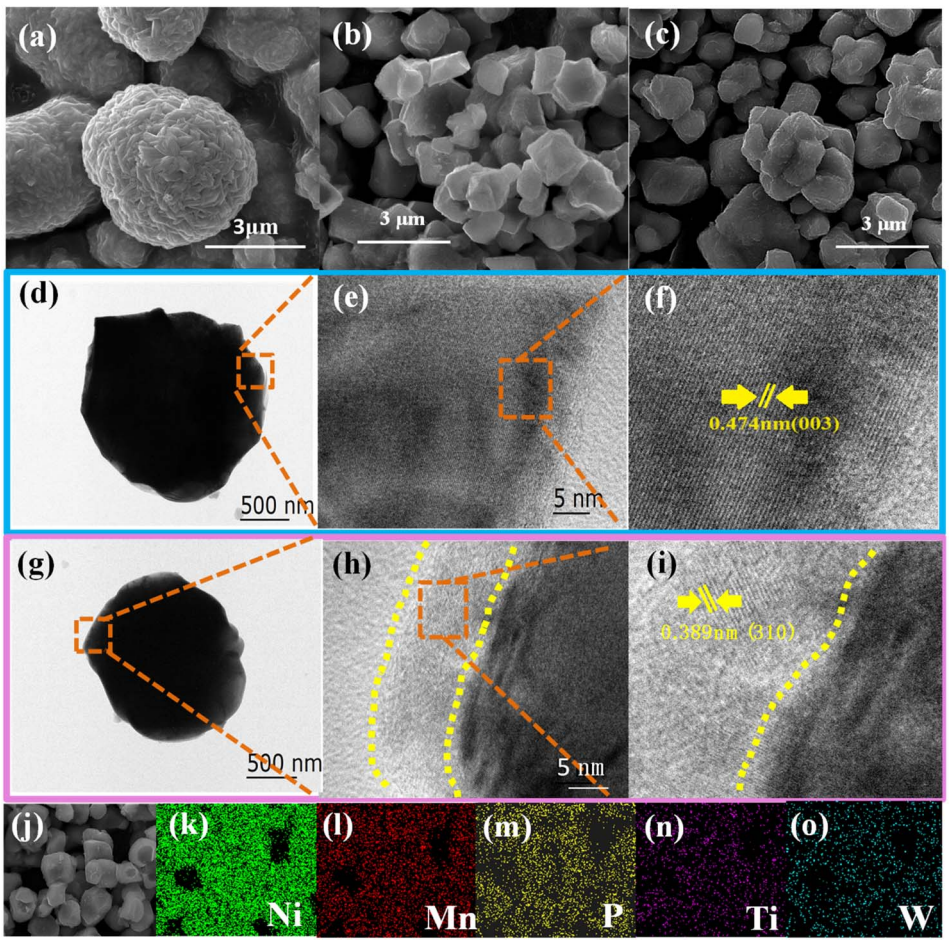


Fig. 2 SEM images of (a) PNM9, (b) SNM9 and (c) SNM9@LWTP0.3; TEM and HRTEM images of (d–f) SNM9 and (g–i) SNM9@LWTP0.3; (j–o) EDS images of SNM9@LWTP0.3.

 

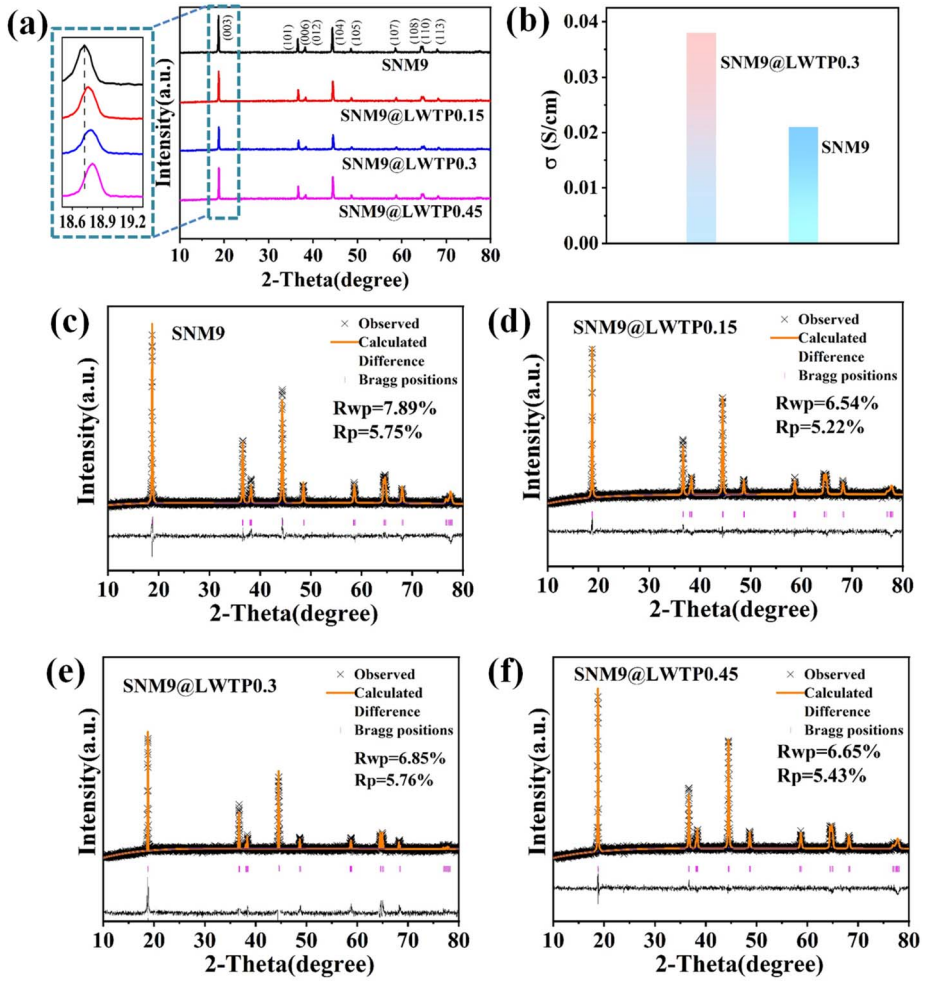


Fig. 3 (a) XRD patterns of the prepared particles; (b) electron conductivity of SNM9 and SNM9@LWTP0.3; Rietveld refinement of (c) SNM9, (d) SNM9@LWTP0.15, (e) SNM9@LWTP0.3, and (f) SNM9@LWTP0.45.

calcination approach is illustrated in Fig. 1. As presented in Fig. 2a, the SNM9 precursor is composed of tridimensional sheets with a particle size of 2–5 μm. After calcination, the precursors turn into single-crystal particles. Both the pristine SNM9 and LWTP-coated SNM9@LWTP0.3 samples show well-defined single-crystal characteristics with average diameters of 2–4 μm (Fig. 2b and c), while moderate particle agglomeration is observed due to sintering effects during high-temperature calcination. The surface of the pristine SNM9 sample is relatively smooth, whereas the LWTP modified SNM9@LWTP0.3 presents a rough surface with uniformly dispersed nanoscale particulates. Elemental distribution analysis through EDS mapping (Fig. 2k–o) confirms the homogeneous dispersion of Ni, Mn, P, Ti, and W across the SNM9@LWTP0.3 surface, confirming the successful formation of a conformal LWTP coating layer.

TEM and HRTEM images of SNM9 and SNM9@LWTP0.3 (Fig. 2d–i) further confirm the presence of the LWTP coating. No coating layer is observed on the surface of SNM9; however, distinct lattice fringes with a spacing of 0.474 nm are clearly visible, corresponding to the (003) crystal plane (Fig. 2d–f). In contrast, a uniform LWTP coating layer with a thickness of 10–15 nm is visibly distributed on the SNM9@LWTP0.3 particles. The measured lattice spacing of 0.389 nm in the coating layer corresponds to the (113) crystallographic planes of LWTP (Fig. 2g–i), providing definitive evidence for successful LWTP layer formation. This continuous LWTP layer effectively isolates the cathode material from direct electrolyte contact, thereby suppressing interfacial side reactions.

Fig. 3a presents the XRD patterns of pristine SNM9 and LWTP-coated single-crystal $LiNi_{0.9}Mn_{0.1}O_2$ cathodes. All samples represent the hexagonal α-$NaFeO_2$ structure ($R\bar{3}m$ space group), with no other impurities.[47] The clear separation of the (006)/(012) and (018)/(110) peaks indicates well organized layered structures in all samples.[48] Notably, the (003) diffraction peaks show a slight shift toward higher angles after LWTP coating. This lattice contraction originates from the incorporation of smaller-radius $Ti^{4+}$ (0.061 nm) and $W^{6+}$ (0.060 nm) ions into the near-surface lattice during the coating process,[49] which strengthens the TM–O bonds and enhances structural stability. The electronic conductivity of SNM9@LWTP0.3 is higher than that of pristine SNM9, owing to the higher

Table 1 The lattice parameters and $I_{(003)}/I_{(104)}$ of SNM9 and SNM9@LWTP

| Sample | $a$ (Å) | $c$ (Å) | $c/a$ | $I_{(003)}/I_{(104)}$ | $Li^+/Ni^{2+}$ occupation rate (%) | $R_{wp}$ (%) | $R_p$ (%) |
|---|---|---|---|---|---|---|---|
| SNM9 | 2.8798 | 14.2125 | 4.9352 | 1.49 | 6.33 | 7.89 | 5.75 |
| SNM9@LWTP0.15 | 2.8739 | 14.1992 | 4.9407 | 1.53 | 6.23 | 6.54 | 5.22 |
| SNM9@LWTP0.3 | 2.8686 | 14.1855 | 4.9450 | 1.57 | 5.98 | 6.85 | 5.76 |
| SNM9@LWTP0.45 | 2.8684 | 14.1812 | 4.9439 | 1.51 | 6.29 | 6.65 | 5.43 |

conductivity of the LWTP coating (Fig. 3b). To calculate the lattice parameters of the SNM9 and SNM9@LWTP cathode materials, the corresponding refinement patterns and results are shown in Fig. 3c–f and Table 1. Both $R_{wp}$ and $R_p$ values of the refined results are less than 10%, indicating that the refined results are reliable.[50] It can be seen from the table that the lattice parameters $a$ and $c$ are reduced after coating, consistent with the incorporation of smaller $Ti^{4+}$ and $W^{6+}$ ions into the crystal structure. Furthermore, the increased $I_{(003)}/I_{(104)}$ intensity ratio in SNM9@LWTP0.3 indicates significantly mitigated $Li^+/Ni^{2+}$ cation mixing, in full agreement with the refinement data. Combined with EDS analysis, these results verify that the LWTP modification not only forms a surface coating but also anchors firmly at the subsurface interface, establishing rapid $Li^+$ transport channels.

XPS analysis was conducted to investigate the surface composition and chemical states of both pristine SNM9 and LWTP-coated SNM9@LWTP0.3 samples (Fig. 4a–g). The survey spectra (Fig. 4a) confirm the presence of characteristic Ni and Mn signals in both materials. In the Ni 2p spectra (Fig. 4b), two spin–orbit doublets appear at 855.3 eV (Ni $2p_{3/2}$) and 872.7 eV (Ni $2p_{1/2}$). The Ni $2p_{3/2}$ peak splits into two typical peaks of $Ni^{2+}$ (854.7 eV) and $Ni^{3+}$ (856.1 eV).[51] Notably, the increased $Ni^{3+}/Ni^{2+}$ ratio in SNM9@LWTP0.3 indicates reduced cation mixing, consistent with XRD results and confirming enhanced surface stability through LWTP modification. The Mn 2p XPS spectra (Fig. 4d) reveal a higher $Mn^{3+}$ content in SNM9@LWTP0.3 compared to SNM9, demonstrating that trace doping of high-valence $Ti^{4+}$ and $W^{6+}$ reduces the oxidation state of Mn. In Fig. 4c, the O 1s spectrum is fitted into two components at 531.4 eV and 529.2 eV, corresponding to surface oxygen species ($Li_2CO_3$/LiOH) and lattice oxygen (metal–O),[52] respectively. The LWTP-coated sample shows a significant increase in metal–O content with concomitant reduction of lithium impurities, demonstrating that the combined effects of LWTP coating and Ti/W doping substantially enhance both crystalline and interfacial structural stability. Moreover, as shown in Fig. 4e–g, the characteristic peaks of Ti 2p, W 4f and P 2p are observed in the SNM9@LWTP0.3 powder sample, which are absent in the pristine sample. The Ti $2p_{3/2}$ and Ti $2p_{1/2}$ spectra displays two peaks located at 458.7 eV and 464.0 eV, corresponding to $Ti^{4+}$.[53] The strong characteristic peaks at 37.2 eV (W $4f_{5/2}$) and 34.9 eV (W $4f_{7/2}$) correspond to $W^{6+}$,[54] and the P 2p peak is detected at 133.8 eV.[55] To further illustrate the distributions of Ti and W, the SNM9@LWTP0.3 sample was etched from the surface to a depth of 50 nm (Fig. 4h and i). The intensity of the Ti 2p and W 4f spectra gradually decreases with depth, confirming that the LWTP protective layer is successfully coated on the surface of SNM9. Simultaneously, the persistent presence of these signals indicates Ti and W doping into the crystal lattice.

### 3.2 Electrochemical testing

Fig. 5 comprehensively evaluates the electrochemical performance of pristine and LWTP-modified $LiNi_{0.9}Mn_{0.1}O_2$ cathodes. As shown in Fig. 5a, the initial charge–discharge profiles at 0.1C (3.0–4.3 V) demonstrate that the optimal SNM9@LWTP0.3 cathode delivers superior initial discharge capacity (206.1 mA h $g^{-1}$) and coulombic efficiency (86.0%) compared to both unmodified SNM9 (204.4 mA h $g^{-1}$, 84.1% CE) and other LWTP-modified samples. This enhancement is attributed to reduced cation mixing and improved $Li^+$ transport pathways enabled by the LWTP modification. Rate capability tests reveal exceptional high-current performance (Fig. 5b), SNM9@LWTP0.3 exhibits the highest rate performance, delivering discharge capacities of 167.8 mA h $g^{-1}$ at 3C compared to 140.2 mA h $g^{-1}$ for pristine SNM9. The enhanced rate performance demonstrates that the LWTP coating effectively improves charge transfer kinetics by enhancing electronic conductivity, accelerating ionic transport, and reducing interfacial polarization. Long-term cycling at 1C (Fig. 5c) shows the LWTP coating's structural stabilization benefits, with SNM9@LWTP0.3 retaining 80.4% capacity after 100 cycles *versus* 70.1% for unmodified SNM9. Fig. 5d and e provide the charging–discharging voltage profiles for selected cycles. LWTP-modified cathodes exhibit significantly reduced voltage decay, resulting from improved polarization characteristics and enhanced interfacial stability. High-voltage testing (4.5 V cutoff) further highlights the coating's advantages, SNM9@LWTP0.3 achieves both higher initial capacity (214.1 *vs.* 208.2 mA h $g^{-1}$) and superior cycling retention (69.2% *vs.* 53.3% after 100 cycles). At an elevated rate of 3C, SNM9@LWTP0.3 maintains 55.6% capacity retention after 100 cycles, while the uncoated cathode rapidly degrades to 36.2%. These improvements stem from the LWTP coating's multifunctional nature: (1) bulk stabilization through Ti/W doping, (2) interfacial protection against side reactions, (3) CEI layer control, and (4) enhanced charge transport properties.

Cyclic voltammetry analysis was systematically performed to investigate the electrochemical reversibility of the electrodes. Measurements were conducted at 0.1 mV $s^{-1}$ for 2 cycles, followed by higher scan rates of 0.3, 0.5, 0.7, and 1.0 mV $s^{-1}$ between 3.0 and 4.3 V (Fig. 6a–d). Three distinct redox peaks were identified, corresponding to characteristic phase transitions from H1 (hexagonal phase) to M (monoclinic phase), M to

 

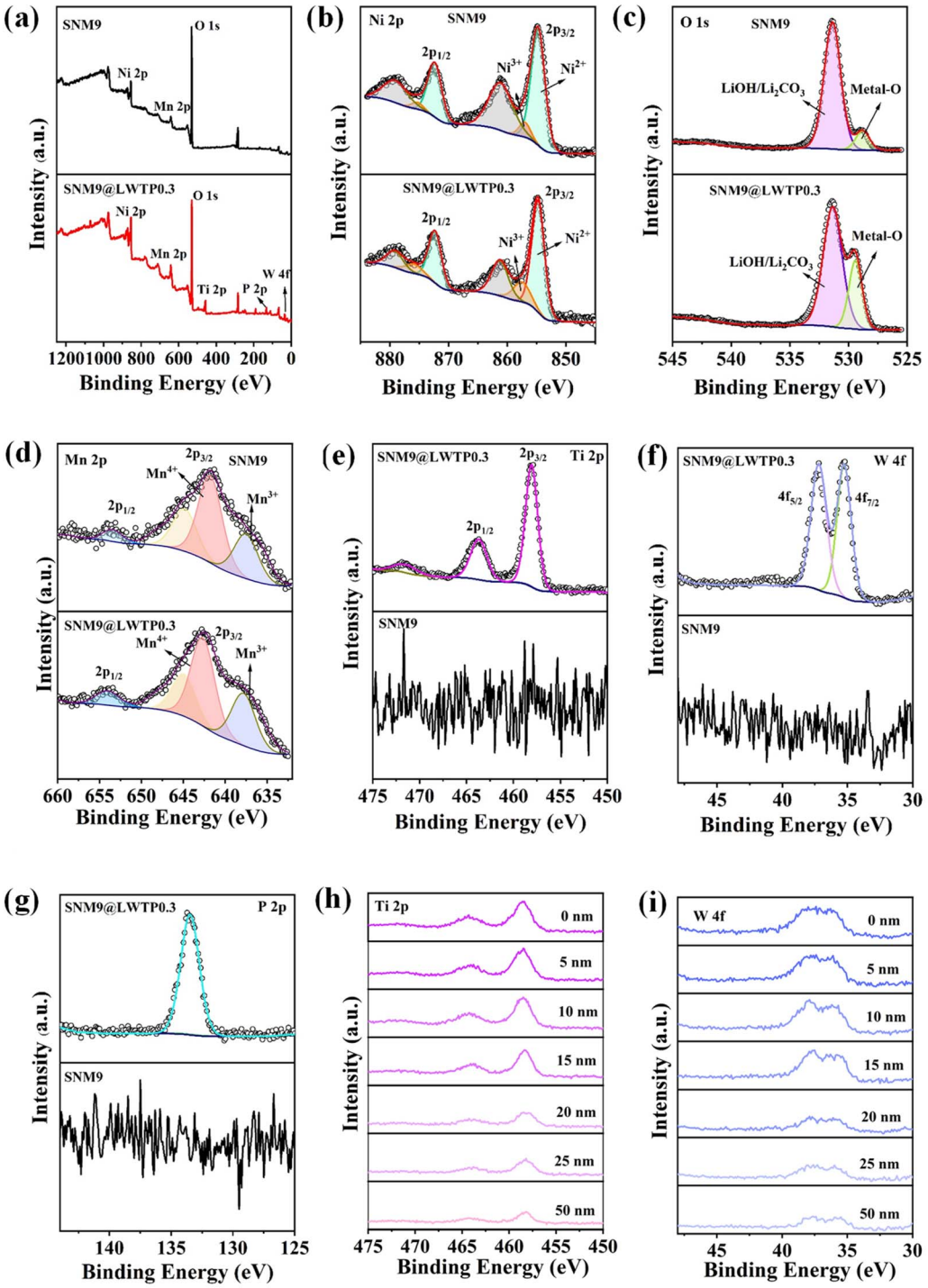


Fig. 4 XPS spectra of the partial elements of SNM9 and SNM9@LWTP0.3: (a) survey spectra, (b) Ni 2p, (c) O 1s, (d) Mn 2p, (e) Ti 2p, (f) W 4f, and (g) P 2p; XPS depth profile of (h) Ti 2p and (i) W 4f.

H2 (hexagonal phase), and H2 to H3 (hexagonal phase).[56] Comparative analysis reveals that SNM9@LWTP0.3 exhibits significantly smaller potential intervals ($\Delta E_p$) between oxidation and reduction peaks during the initial cycle (Fig. 6a and b), indicating reduced electrode polarization. This improvement is attributed to the dual functionality of the LWTP coating enhancing $Li^+$ migration kinetics and retaining redox reaction reversibility by stabilizing the electrode–electrolyte interface. At increased scan rates (Fig. 6c and d), both materials demonstrate the expected rise in peak currents; however, SNM9@LWTP0.3 shows markedly less peak position deviation compared to the substantial shifts observed in unmodified SNM9. This

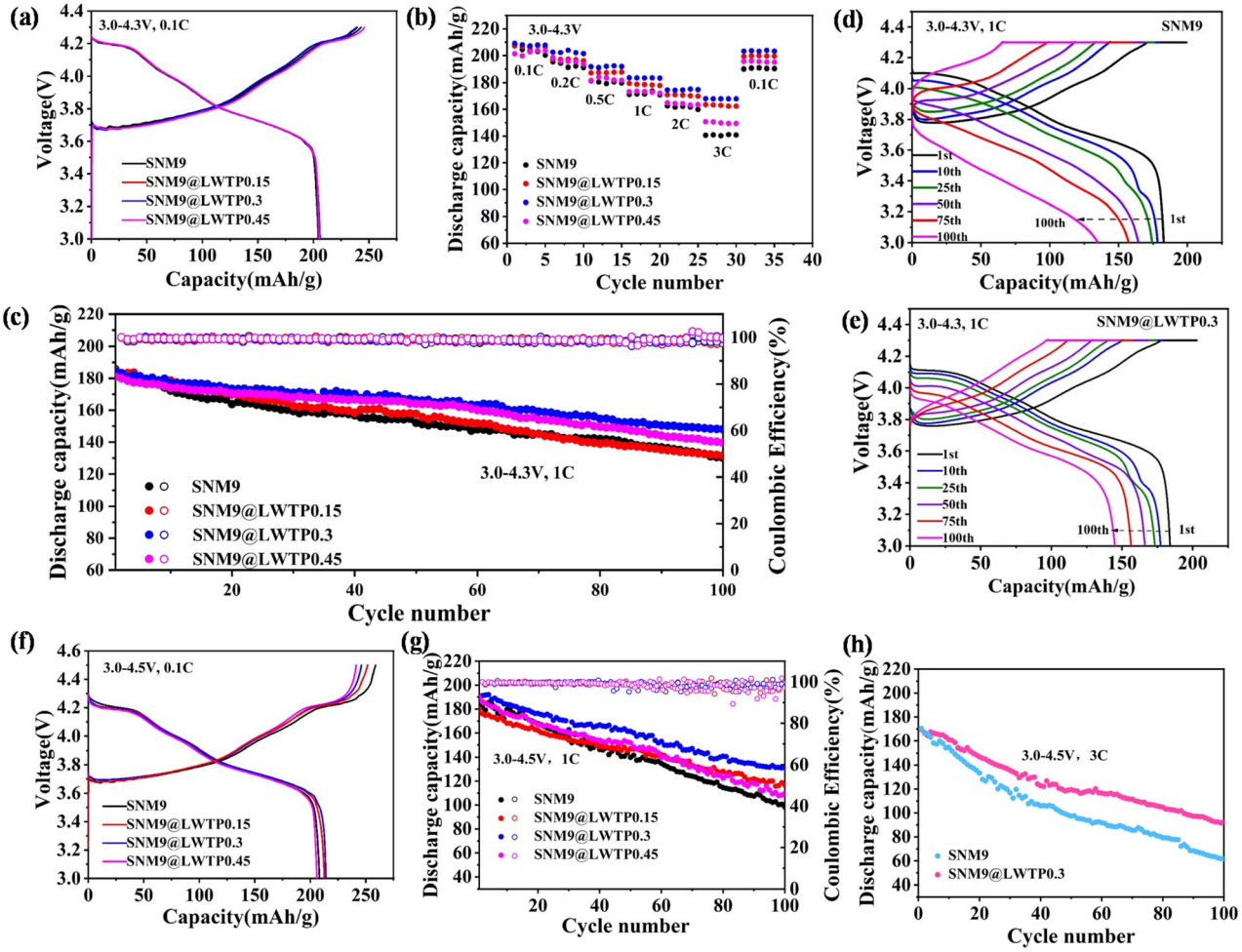


Fig. 5 (a) The initial charging–discharging curves at 0.1C between 3.0 and 4.3 V; (b) rate performances between 3.0 and 4.3 V; (c) cycling performances of SNM9 and SNM9@LWTP at 1C between 3.0 and 4.3 V; (d and e) the charging–discharging performances of SNM9 and SNM9@LWTP0.3 during different number of cycles at 1C between 3.0 and 4.3 V; (f) the initial charging–discharging curves at 0.1C; (g) cycling performances of SNM9 and SNM9@LWTP at 1C between 3.0 and 4.5 V; (h) cycling performances of SNM9 and SNM9@LWTP0.3 at 3C between 3.0 and 4.5 V.

pronounced peak stability in the coated sample reflects its superior resistance to polarization effects and enhanced interfacial stability, indicating that the LWTP coating can reduce charge transfer resistance and simultaneously improve lithium transport kinetics. These synergistic effects directly correlate with the observed enhancements in cycling performance and rate capability.

To elucidate the impact of the LWTP coating on $Li^+$ diffusion kinetics and interfacial stability, EIS measurements were conducted on both SNM9 and SNM9@LWTP0.3 electrodes before and after cycling (Fig. 7a and b). The Nyquist plots, obtained after the 1st and 100th cycles at 4.5 V, exhibit three distinct features: (1) a high-frequency semicircle corresponding to SEI film resistance ($R_{sf}$), (2) an intermediate-frequency semicircle representing charge transfer resistance ($R_{ct}$), and (3) a low-frequency Warburg impedance ($Z_w$) associated with $Li^+$ diffusion.[57] The analysis reveals that the $R_{ct}$ of pristine SNM9 increases dramatically from 65.7 Ω to 193.6 Ω after 100 cycles, whereas SNM9@LWTP0.3 demonstrates superior interfacial stability, with $R_{ct}$ increasing only from 52.8 Ω to 108.6 Ω. This significant reduction in charge transfer resistance highlights the LWTP coating's ability to mitigate electrode/electrolyte side reactions, suppress disordered rock-salt phase formation, and inhibit excessive CEI growth, collectively enhancing interfacial stability and $Li^+$ diffusion kinetics.

$$D_{Li^+} = \left(\frac{RT}{\sqrt{2}An^2F^2\sigma C}\right)^2 \quad (1)$$

$$Z' = R_s + R_{ct} + \sigma\omega^{-1/2} \quad (2)$$

Furthermore, $Li^+$ diffusion coefficients ($D_{Li^+}$) were calculated using eqn (1) and (2),[58] where $R$ represents the gas constant, $T$ is the absolute temperature, $A$ is the surface area of the electrode, $n$ is the number of electrons lost per molecule in the electrochemical reaction, $F$ is the Faraday constant, and $C$ is the concentration of $Li^+$. $\sigma$ (Warburg coefficient) was derived from

 

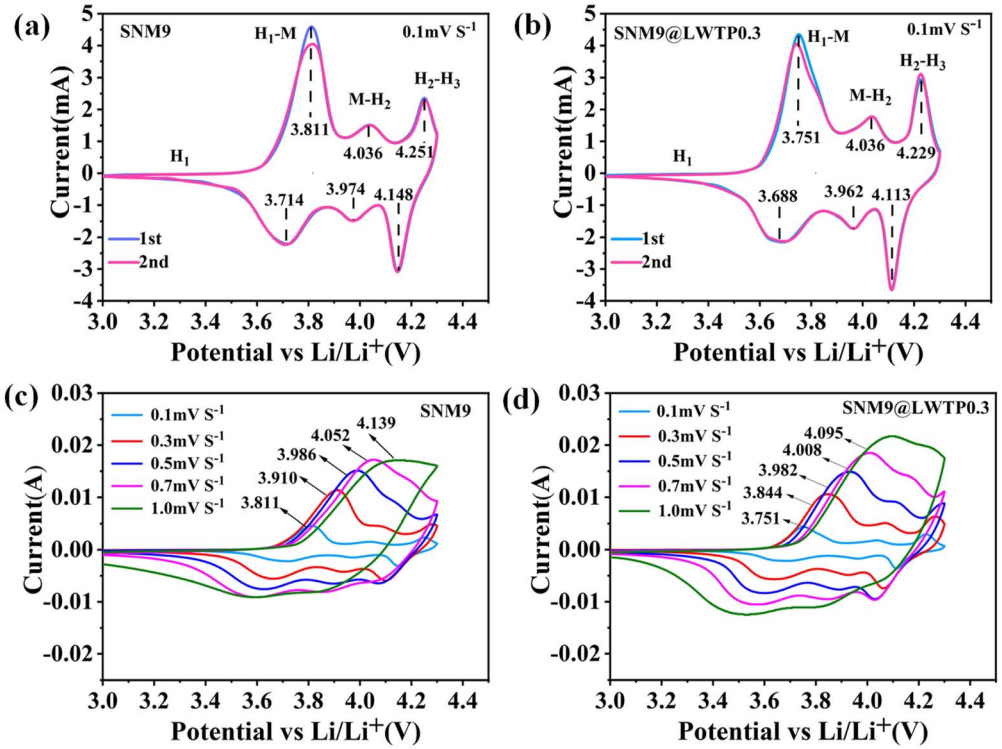


Fig. 6 CV curves of SNM9 and SNM9@LWTP0.3 at 0.1 mV $s^{-1}$ for 2 cycles: (a) SNM9 and (b) SNM9@LWTP0.3; CV curves of SNM9 and SNM9@LWTP0.3 at 0.1–1.0 mV $s^{-1}$: (c) SNM9 and (d) SNM9@LWTP0.3.

the linear fitting of $Z'$ *vs.* $\omega^{-0.5}$ (Fig. 7c).[59] The $D_{Li^+}$ values for SNM9 and SNM9@LWTP0.3 were determined to be $3.79 \times 10^{-12}$ $cm^2$ $s^{-1}$ and $3.21 \times 10^{-11}$ $cm^2$ $s^{-1}$, respectively. The order-of-magnitude improvement in $D_{Li^+}$ for the coated sample directly correlates with its superior electrochemical performance, including enhanced rate capability and cycling stability, underscoring the critical role of LWTP in optimizing interfacial charge transfer and $Li^+$ transport.

The galvanostatic intermittent titration technique (GITT) was employed to quantitatively evaluate $Li^+$ diffusion kinetics during electrochemical operation (0.1C, 3.0–4.3 V). As shown in Fig. 7d and e, the GITT profiles for SNM9@LWTP0.3 exhibit

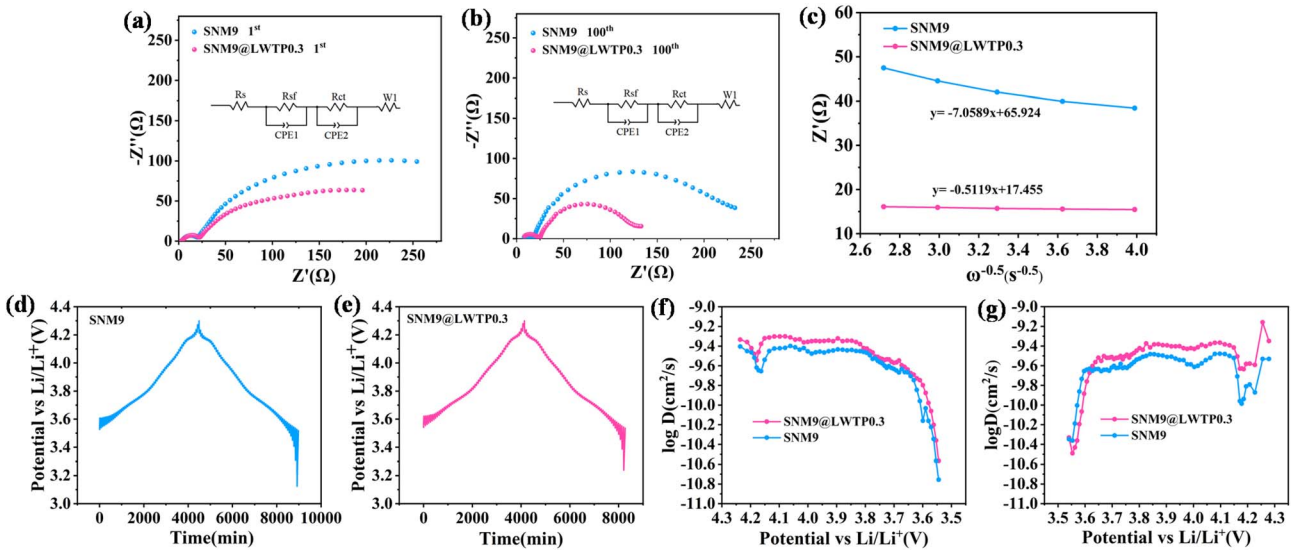


Fig. 7 Nyquist plots of cathodes in a voltage range of 3.0–4.5 V: (a) the initial cycle and (b) after 100 cycles; (c) the profiles of $Z'$ and $\omega^{-1/2}$; (d and e) GITT curves of SNM9 and SNM9@LWTP0.3 cells during charging/discharging in a voltage range of 3.0–4.3 V; the profiles of $Li^+$ diffusion coefficients of SNM9 and SNM9@LWTP0.3 samples for the charge process (f) and discharge process (g).

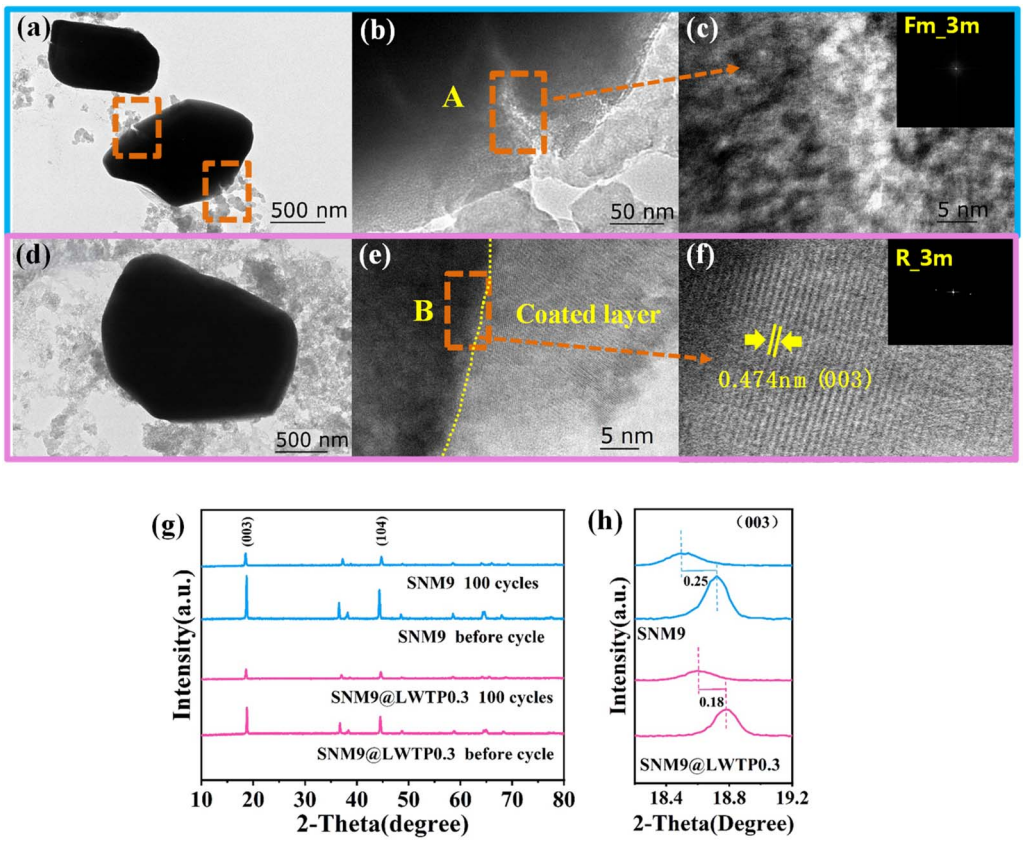


Fig. 8 TEM and HRTEM images of cathodes after 100 cycles in the voltage range of 3.0–4.5 V: (a–c) SNM9 and (d–f) SNM9@LWTP0.3; XRD patterns of SNM9 and SNM9@LWTP0.3 after 100 cycles in the voltage range of 3.0–4.5 V: (g) full scan and (h) the enlarged (003) peaks.

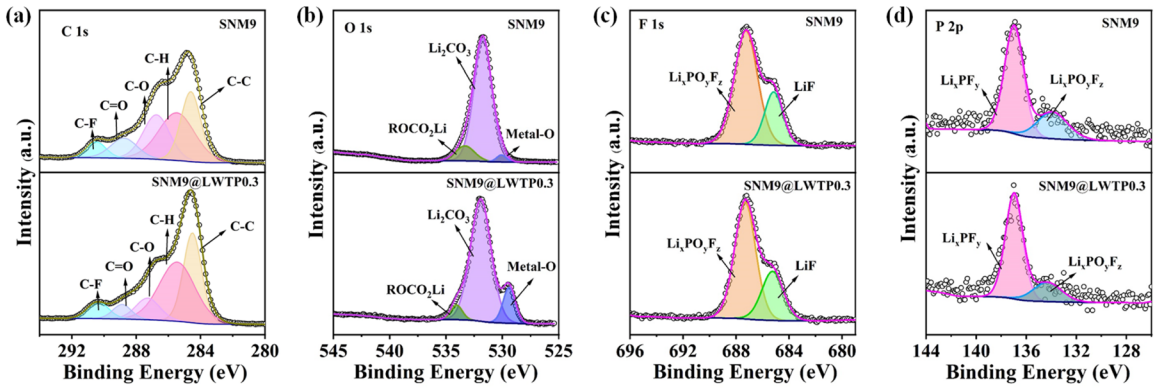


Fig. 9 XPS spectra of SNM9 and SNM9@LWTP0.3 after 100 cycles in the voltage range of 3.0–4.5 V: (a) C 1s, (b) O 1s, (c) F 1s, and (d) P 2p.

significantly reduced polarization and improved voltage stability during both charge and discharge processes compared to pristine SNM9. The $Li^+$ diffusion coefficient ($D_{Li^+}$) was calculated using eqn (3):[60]

$$D_{Li} = \frac{4}{\pi\tau}\left(\frac{mV_m}{MS}\right)^2\left(\frac{\Delta E_S}{\Delta E_\tau}\right)^2\left(\tau \ll \frac{L^2}{D_{Li}}\right) \quad (3)$$

where $\tau$ is the charging time, $V_m$ is the molar volume of the materials, $m$ is the mass of the active substance, $M$ represents the molecular weight of the electrode materials, $A$ is the specific surface area of the electrode materials, $\Delta E_\tau$ is the voltage change caused by constant current charging, and $\Delta E_S$ is the voltage change caused by the impulse. Fig. 7f and g presents the calculation values of the $Li^+$ diffusion coefficient ($D_{Li^+}$) during the charge/discharge process. It can be found that SNM9@LWTP0.3 exhibits superior $D_{Li^+}$ compared to SNM9; SNM9@LWTP0.3 demonstrates consistently higher $Li^+$ diffusivity throughout the entire charge/discharge window. This methodological consistency confirms that the LWTP coating

 

Table 2 The atomic wt % of C, O, F, and P remaining after the cycling for the electrodes

| Element | C (wt %) | O (wt %) | F (wt %) | P (wt %) |
|---|---|---|---|---|
| SNM9 | 47.08 | 28.54 | 23.46 | 0.92 |
| SNM9@LWTP0.3 | 50.90 | 26.41 | 21.85 | 0.84 |

can create favorable $Li^+$ transport pathways, reduce interfacial resistance, and maintain structural integrity during cycling.

### 3.3 Analysis of cycled cathodes

TEM and HRTEM were employed to further study the structural changes of the cycled cathodes after 100 cycles at 1C (3.0–4.5 V). The uncoated SNM9 cathode exhibits microcracks within the particles (Fig. 8a–c), which provide microchannels for the electrolyte to corrode the internal structure. Disordered NiO-type rock-salt phases ($Fm\bar{3}m$ space group) can be observed along the intragranular crack, primarily caused by severe side reactions involving high-valence $Ni^{4+}$ during deep charge/discharge. This leads to increased internal resistance and capacity fading.[12] In contrast, SNM9@LWTP0.3 retains its pristine single-crystal morphology ($R\bar{3}m$ space group) with intact particle integrity and no observable cracking, while preserving a stable coating–electrode interface (Fig. 8d–f).

To systematically evaluate the long-term structural stability under high-voltage operation (3.0–4.5 V), we conducted *ex situ* XRD analysis on cycled SNM9 and SNM9@LWTP0.3 electrodes after 100 cycles (Fig. 8g and h). Both samples exhibit reduced diffraction peak intensities and a low-angle shift of the (003) reflection, indicating *c*-axis expansion.[61] This behavior is characteristic of lattice strain accumulation during prolonged cycling. SNM9@LWTP0.3 demonstrates a significantly smaller (003) peak displacement, confirming that the LWTP coating layer effectively suppresses anisotropic lattice distortion, mitigates microcrack formation, and maintains layered structure integrity.

Additionally, XPS measurements were conducted to elucidate the interfacial stability of cycled electrodes after 100 cycles at 4.5 V. In the C 1s spectra (Fig. 9a), the peak at 284.5 eV corresponds to C–C in acetylene black. The peak at 285.6 eV is related to the C–H bonds from alkyl carbonates and PVDF, while the peak at 290.4 eV is assigned to C–F in PVDF. The C–O (286.7 eV) and C=O (288.9 eV) peaks originate from the decomposition products of carbonate electrolyte, such as $ROCO_2Li$, ROLi and $Li_2CO_3$.[33] Compared to SNM9, the reduced peak intensity observed in SNM9@LWTP0.3 suggests suppressed electrolyte

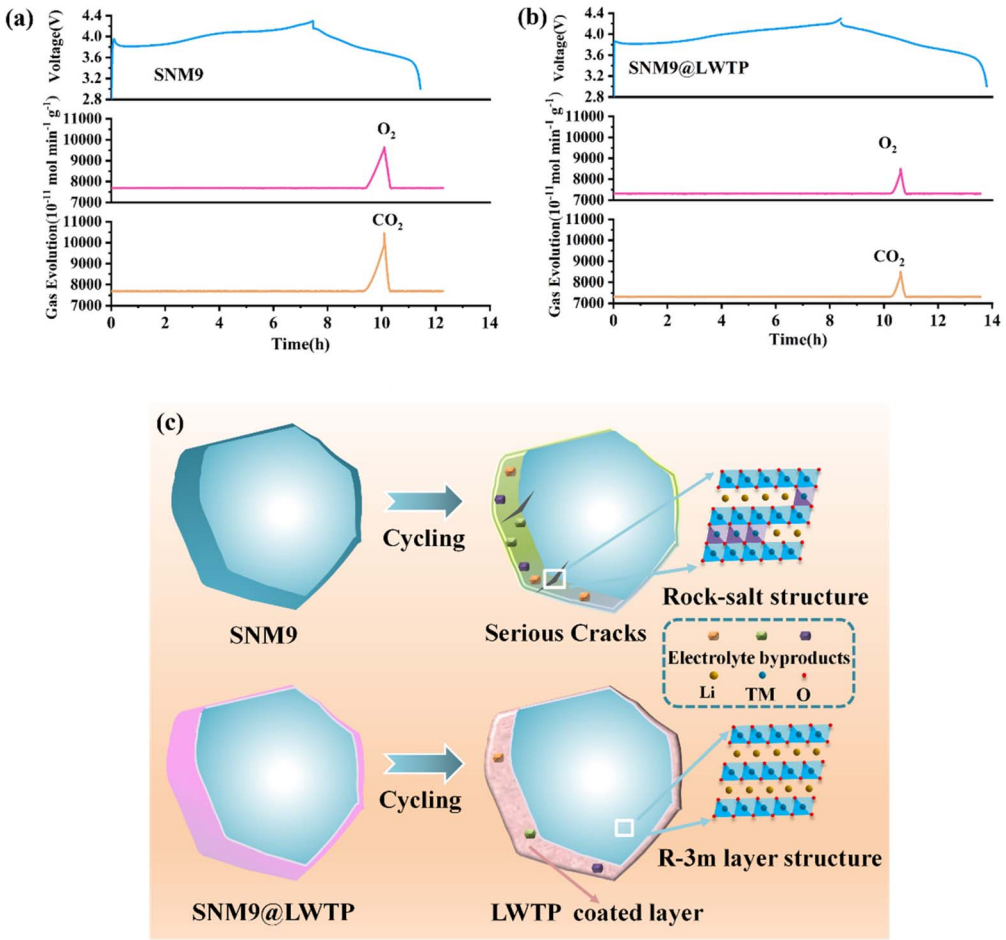


Fig. 10 DEMS of cathodes: (a) SNM9 and (b) SNM9@LWTP0.3; (c) schematic diagram of the effect of the LWTP coating on the SNM9 material.

decomposition. The O 1s spectrum (Fig. 9b) shows three main peaks located at around 534 eV, 532 eV, and 529 eV, corresponding to $ROCO_2Li$, $Li_2CO_3$ and metal–oxygen (M–O) bonds, respectively.[62] Notably, SNM9@LWTP0.3 demonstrates a higher M–O content and a reduction in $ROCO_2Li$, indicating that the LWTP coating layer effectively maintains structural integrity and suppresses side reactions. The F 1s XPS spectra (Fig. 9c) reveal substantially more intense LiF signatures in pristine SNM9 than in SNM9@LWTP0.3, revealing critical coating effects on significant suppression of electrolyte decomposition, effective limitation of CEI layer growth, and reduction of $Li^+$ diffusion barriers. Furthermore, the P 2p spectrum (Fig. 9d) indicates that more $Li_xPO_xF_2$ species accumulate on the surface of SNM9, accelerating electrolyte degradation and increasing interfacial impedance. Elemental content analysis (C, O, F, and P) (Table 2) confirms that SNM9@LWTP0.3 exhibits lower F and P content than SNM9. Notably, the CEI layer of SNM9 shows a clear trend of increased formation of LiF, $Li_2CO_3$, $ROCO_2Li$, and ROLi, further highlighting the protective effect of the LWTP coating.

Differential electrochemical mass spectrometry (DEMS) was used to evaluate gas evolution during electrochemical cycling (0.3C, 3.0–4.3 V). As shown in Fig. 10a and b, while neither SNM9 nor SNM9@LWTP0.3 exhibited detectable $O_2$ or $CO_2$ release during charging, both materials showed significant gas evolution during discharge. The observed $O_2$ originates from lattice oxygen loss due to structural instability, while $CO_2$ generation results from surface reactive oxygen species and subsequent electrolyte oxidation.[63,64] Critically, SNM9@LWTP0.3 demonstrates lower $O_2$ emission and $CO_2$ production. These results indicate that the LWTP coating stabilizes the oxygen sublattice through Ti–O and W–O bonding, limits surface oxidative reactions, and thereby preserves structural integrity during cycling.

The mechanism of the LWTP coating's protective effect on SNM9 after long-term cycling is shown in Fig. 10c. During high-voltage cycling, uncoated SNM9 cathodes undergo progressive degradation. At the interface, direct electrolyte attack and CEI growth occur. In the bulk material, anisotropic phase transition strain induces microcracks at grain boundaries, which propagate into intragranular fractures. Concurrently, surface reconstruction to a disordered rock-salt phase occurs alongside irreversible oxygen loss. These coupled degradation modes collectively accelerate capacity fade. However, the LWTP coating protects the interface from electrolyte corrosion, buffers anisotropic strain and prevents microcrack propagation, thus maintaining excellent structural integrity. It retains the fast $Li^+$ diffusion channel, stabilizes the oxygen framework and reduces the charge transfer resistance. Synergistically, these effects significantly enhance the electrochemical properties of the material.

# 4 Conclusions

This work presents a multifunctional LWTP coating strategy that simultaneously stabilizes the bulk structure, interface, and oxygen stability challenges of single-crystal $LiNi_{0.9}Mn_{0.1}O_2$ cathodes. The LWTP coating achieves remarkable structural stabilization by reducing $Li^+/Ni^{2+}$ cation mixing, suppressing rock-salt phase formation, and effectively mitigating intrinsic anisotropic structural degradation during high-voltage operation. It provides exceptional interfacial protection by reducing charge transfer resistance and forming an ultrathin protective barrier that prevents electrolyte corrosion and microcrack propagation. Furthermore, DEMS analysis confirms the coating's oxygen buffering capability. The optimized 0.3 wt % LWTP-coated cathode delivers outstanding electrochemical performance, including a high capacity of 214.1 mA h $g^{-1}$ at 4.5 V with 69.2% retention after 100 cycles, superior rate capability (167.8 mA h $g^{-1}$ at 3C, 4.3 V, representing a 19.7% improvement over the uncoated cathode), and excellent cycling stability (80.4% capacity retention after 100 cycles at 1C, 4.3 V). Unlike conventional coatings, LWTP actively participates in charge transfer through its fast-ion-conducting network, providing triple protection against structural degradation, oxygen loss, and mechanical strain. This work establishes a new paradigm for designing stable high-voltage cathodes.

# Data availability

The data supporting this article are not from any other published articles, books, web pages, or databases. They are all obtained from the related electrochemical workstations, battery testers, and related characterization equipment; therefore, the data supporting the findings of this article are available from the corresponding author upon reasonable request.

# Author contributions

Hailan Feng: conceptualization, visualization, methodology, writing-original draft. Yuxing Xu: data curation, writing-review & editing. Ying Hou: formal analysis, visualization, investigation. Fuchang Zhuge: resources, funding acquisition. Qiangqiang Tan: resources, supervision, validation, funding acquisition.

# Conflicts of interest

The authors declare that they have no known competing financial interests or personal relationships that could have appeared to influence the work reported in this paper.

# Acknowledgements

This work was financially supported by the General Project of Beijing Natural Science Foundation (2222030), the Key R&D Projects in Gansu Province (22YF7GD193), and the Project of Hebei Academy of Science (24709).

# References

1 T. H. Mengesha, J. Jeyakumar, Y. B. Hendri, Y. S. Wu, C. C. Yang, Q. T. Pham, C. S. Chern, G. Brunklaus,

 

M. Winter and B. J. Hwang, *ACS Appl. Mater. Interfaces*, 2024, **16**, 21034–21049.
2 M. Kim, E. Seok, J. Park, S. Lee, H. Kang, M. Ku, C. K. Yoon, H. Jung and W. Choi, *Chem. Eng. J.*, 2022, **450**(P1), 137939.
3 B. Hu, J. Q. Peng, D. M. Liu, M. L. Wu, Y. Y. Wei, B. Huang, Y. W. Li, S. H. Xiao and R. Wang, *ACS Appl. Energy Mater.*, 2023, **6**, 5318–5330.
4 X. M. Fan, Y. D. Huang, H. X. Wei, L. B. Tang, Z. J. He, C. Yan, J. Mao, K. H. Dai and J. C. Zheng, *Adv. Funct. Mater.*, 2021, **32**, 2109421.
5 W. Z. Liu, Z. Q. Zheng and Y. K. Zheng, *J. Alloys Compd.*, 2023, **963**, 171130.
6 A. Jungyoung, L. Yongho, J. K. Hyojeong, L. Seokjae, H. Seulki, L. Byong-June, K. Jeonghan and Y. Taeeun, *ACS Sustain. Chem. Eng.*, 2023, **11**, 4342–4352.
7 Y. Jin, Z. L. Yang, H. Y. Kan, Y. C. Zha, C. C. Li, Q. Meng, P. Dong and Y. J. Zhang, *Ceram. Int.*, 2024, **50**, 24872–24880.
8 Z. Wang, H. Zhu, H. Yu, T. Zhang, Y. Hu, H. Jiang and C. Li, *Chin. Chem. Lett.*, 2023, **34**, 107718.
9 L. Ni, S. Zhang, A. Di, W. Deng, G. Zou, H. Hou and X. Ji, Challenges and Strategies Towards Single-crystalline Ni-rich Layered Cathodes, *Adv. Energy Mater.*, 2022, **12**, 2201510.
10 W. Wang, Y. Zhou, B. Zhang, W. Huang, L. Cheng, J. Wang, X. He, L. Yu, Z. Xiao, J. Wen, T. Liu, K. Amine and X. Ou, *ACS Nano*, 2024, **18**, 8002–8016.
11 J. Yan, Z. L. Yang, H. Y. Kan, Y. C. Zha, C. C. Li, Q. Meng, P. Dong and Y. J. Zhang, *Ceram. Int.*, 2024, **50**, 24872–24880.
12 J. X. Shen, B. Zhang, W. Y. Huang, X. Li, Z. M. Xiao, J. Wang, T. Zhou, J. G. Wen, T. C. Liu, K. Amine and X. Ou, *Adv. Funct. Mater.*, 2023, **33**, 2300081.
13 L. W. Liang, M. S. Su, Z. F. Sun, L. X. Wang, L. R. Hou, H. D. Liu, Q. B. Zhang and C. Z. Yuan, *Sci. Adv.*, 2024, **10**, 4472.
14 L. S. Ni, S. Zhang, A. D. Di, W. T. Deng, G. Q. Zou, H. S. Hou and X. B. Ji, *Adv. Energy Mater.*, 2022, **12**(31), 2201510.
15 J. J. Liu, Y. F. Yuan, J. H. Zheng, L. G. Wang, J. Ji, Q. Zhang, L. Yang, Z. Y. Bai and J. Lu, *Angew. Chem., Int. Ed.*, 2023, **62**, 202302547.
16 N. Voronina, Y. K. Sun and S. T. Myung, *ACS Energy Lett.*, 2020, **5**, 1814–1824.
17 X. H. Meng, T. Lin, H. C. Mao, J. L. Shi, H. Y. Sheng, G. Zou, M. Fan, K. C. Jiang, R. J. Xiao, D. D. Xiao, L. Gu, L. J. Wan and Y. G. Guo, *J. Am. Chem. Soc.*, 2022, **144**(25), 11338–11347.
18 X. Ou, T. C. Liu, W. T Zhong, X. M. Fan, X. Y. Guo, X. J. Huang, L. Cao, J. H. Hu, B. Zhang, Y. S. Chu, G. R. Hu, Z. Lin, M. Dahbi, J. Alami, K. Amine, C. H. Yang and J. Lu, *Nat. Commun.*, 2022, **13**, 2319.
19 Y. Bi, J. Tao, Y. Wu, L. Li, Y. Xu, E. Hu, B. Wu, J. Hu, C. Wang, J. G. Zhang, Y. Qi and J. Xiao, *Science*, 2020, **370**, 1313–1317.
20 J. Yan, Z. L Yang, H. Y. Kan, Y. C. Zha, C. C. Li, Q. Meng, P. Dong and Y. Y. Zhang, *Chem. Eng. J.*, 2024, **498**, 155617.
21 L. Cheng, Y. N. Zhou, B. Zhang, W. Wang, L. Ming, Z. M. Xiao and X. Ou, *Chem. Eng. J.*, 2023, **452**, 139336.
22 Z. Zhang, B. Hong, M. Yi, X. Fan, Z. Zhang, X. Huang and Y. Lai, *Chem. Eng. J.*, 2022, **445**, 136825.
23 Y. L. Xu, T. Y. Pan and F. C. Liu, *J. Electroanal. Chem.*, 2022, **914**, 116286.
24 G. S. Zhou, Y. W. Wei and H. W. Li, *Part. Part. Syst. Charact.*, 2022, **39**(7), 2200061.
25 L. Z. You, Y. Wen and G. X. Li, *J. Mater. Chem. A*, 2022, **10**(10), 5631–5641.
26 B. Huang, M. Wang and X. W. Zhang, *J. Alloys Compd.*, 2020, **830**, 154619.
27 W. D. Bao, G. N. Qian and L. Q. Zhao, *Nano Lett.*, 2020, **20**(12), 8832–8840.
28 L. M. Ou, S. H. Nong and R. X. Yang, *Nano Mater.*, 2022, **12**(8), 1324.
29 M. H. Lia, L. Cheng, B. Zhang, P. Deng, Z. M. Xiao, L. Ming, Y. Zhao, B. H. Xu and X. Ou, *J. Alloys Compd.*, 2022, **907**, 164489.
30 Y. Y. Wei, B. Hu, J. Q. Peng, L. Zhang, J. F. Huang, H. Y. Tang, B. Huang, Y. W. Li, S. J. Chen and S. H. Xiao, *J. Electroanal. Chem.*, 2023, **932**, 117202.
31 H. X. Xie, Z. Y. Liang, D. Luo, L. Zhang, J. F. Huang, H. Y. Tang, B. Huang, Y. W. Li, S. J. Chen and S. H. Xiao, *Chem. Commun.*, 2020, **56**(80), 12009–12012.
32 Y. H. Du, H. Sheng, X. H. Meng, X. D. Zhang, Y. G. Zou, J. Y. Liang, M. Fan, F. Y. Wang, J. L. Tang, F. F. Cao, J. L. Shi, X. F. Cao and Y. G. Guo, *Nano Energy*, 2022, **94**, 106901.
33 C. M. Jiao, M. Wang, B. Huang, M. X. Zhang, G. D. Xu, Y. X. Liu, Y. F. Zhao and X. B. Hu, *J. Alloys Compd.*, 2023, **937**, 168389.
34 S. Jamil, G. Wang, L. Yang, X. Xie, S. Cao, H. Liu, B. B. Chang and X. Y. Wang, *J. Mater. Chem. A*, 2020, **8**(40), 21306–21316.
35 L. M. Babulal, S. H. Wu and C. C. Yang, *Ceram. Int.*, 2020, **46**(14), 22606–22618.
36 X. L. Li, L. B Jin, D. W. Song, H. Zhang, X. Shi, Z. Wang, L. Zhang and L. Y. Zhu, *J. Energy Chem.*, 2019, **40**, 39–45.
37 Y. L. Xu, T. Y. Pan, F. C Liu, P. Zhao, X. M. Jiang and C. Y. Xiong, *J. Electroanal. Chem.*, 2022, **914**, 116286.
38 J. Y. Ma, X. Huang, R. J. Huang, Y. Tang, S. Y. Huang, Y. H. Wang, B. Huang, J. W. Yang, Y. W. Li, M. Qin and S. H. Xiao, *J. Mater. Chem. A*, 2025, **13**, 15858–15870.
39 M. X. Liu, G. H. Guo, J. X. Ji, R. Zhu and T. Zhou, *Ionics*, 2023, **29**(7), 2563–2572.
40 W. Hu, S. W. Zhong, X. F. Rao, T. T. Yan and M. Zeng, *Front. Energy Res.*, 2022, **10**, 869404.
41 Y. Zhang, Z. H. Zhang, Y. K. Tang, D. Z. Jia, Y. D. Huang, W. K. Pang, Z. P. Guo and Z. Zhou, *Adv. Funct. Mater.*, 2019, **29**(17), 1807895.
42 J. W. Choi and J. W. Lee, *J. Power Sources*, 2016, **307**, 63–68.
43 V. Thangadurai and W. Weppner, *Ionics*, 2006, **12**(1), 81–92.
44 M. J. Hou, F. Liang, K. F. Chen, Y. N. Dai and D. F. Xue, *Nanotechnology*, 2020, **31**(13), 132003.
45 C. R. Mariappan, C. Yada, F. C. Rosciano and B. Roling, *J. Power Sources*, 2011, **196**(15), 6456–6464.
46 X. M. Fan, X. Ou, W. G. Zhao, B. Zhang, J. F. Zhang, L. F. Zou, L. Seidl, Y. Z. Li, G. R. Hu, C. Battaglia and Y. Yang, *Nat. Commun.*, 2021, **12**(1), 5320.
47 Y. Shi, M. H. Zhang, Y. S. Meng and Z. Chen, *Adv. Energy Mater.*, 2019, **9**, 1900454.
48 M. Mao, B. Huang, Q. Li, C. Wang, Y. B. He and F. Kang, *Nano Energy*, 2020, **78**, 105282.

49 C. P. Liang, F. T. Kong, R. C. Longo, C. X. Zhang, Y. F. Nie, Y. P. Zheng and K. Cho, *J. Mater. Chem. A*, 2017, **5**(48), 25303–25313.
50 G. T. Park, H. H. Ryu, N. Y. Park, C. S. Yoon and Y. K. Sun, *J. Power Sources*, 2019, **442**, 227242.
51 Y. F. Su, Y. Q. Yang, L. Chen, Y. Lu, L. Y. Bao, G. Chen, Z. R. Yang, Q. Y. Zhang, J. Wang, R. J. Chen, S. Chen and F. Wu, *Electrochim. Acta*, 2018, **292**, 217–226.
52 Y. H. Zong, Z. X. Guo, T. T. Xu, C. Liu, Y. H. Li and G. Yang, *Int. J. Energy*, 2020, **44**(11), 8532–8541.
53 Z. F. Yang, H. F. Yu and Y. J. Hu, *Chem. Eng. Sci.*, 2021, **231**, 116297.
54 Z. X. Zhou, X. Q. Cheng, P. J. Zuo, C. Y. Du, Y. Z. Gao and G. P. Yin, *J. Power Sources*, 2017, **361**, 227–236.
55 U. H. Kim, N. Y. Park, G. T. Park, H. Kim, C. S. Yoon and Y. K. Sun, *Energy Storage Mater.*, 2020, **33**, 399–407.
56 R. Robert, C. Bünzli, E. J. Berg and P. Novák, *Chem. Mater.*, 2015, **27**(2), 526–536.
57 F. J. Zhu, Y. Shi, G. R. Hu, Z. D. Peng, Y. B. Cao, Q. Sun, Z. C. Xue, Y. J. Zhang and K. Du, *Ceram. Int.*, 2021, **47**(3), 3070–3078.
58 Z. L. Zhang, D. H. Chen and C. K. Chang, *RSC Adv.*, 2017, **7**(81), 51721–51728.
59 T. L. Zhao, Y. Meng, R. X. Ji, F. Wu, L. Li and R. J. Chen, *J. Alloys Compd.*, 2019, **811**, 152060.
60 W. Weppner and R. A. Huggins, *J. Electrochem. Soc.*, 1977, **124**(10), 1569–1578.
61 B. Huang, M. Wang and X. W. Zhang, *J. Alloys Compd.*, 2020, **830**, 154619.
62 T. H. Mengesha, J. Jeyakumar, Y. B. Hendri, Y. S. Wu, C. C. Yang, Q. T. Pham, C. S. Chern, G. Brunklaus, M. Winter and B. J. Hwang, *ACS Appl. Mater. Interfaces*, 2024, **16**, 21034–21049.
63 J. Inamoto, K. J. Baskoro and Y. Matsuo, *J. Electrochem. Soc.*, 2023, **170**(1), 010513.
64 B. B. Chu, R. Y. Xu, G. X. Li, J. Y. Chen, Z. J. Xu, T. Huang, B. Wang and A. Yu, *J. Power Sources*, 2023, **577**, 233260.

 